Cracks and Fingers: Dynamics of ductile fracture in an aqueous foam

Peter S. Stewart[*], Sascha Hilgenfeldt[†]

March 27, 2017

Abstract

Fracture of a quasi-two-dimensional aqueous foam by injection of air can occur via two distinct mechanisms, termed brittle and ductile, which are analogous to crack modes observed for crystalline atomic solids such as metals. In the present work we focus on the dynamics and morphology of the ductile process, in which no films between bubbles are broken. A network modeling approach allows detailed analysis of the foam morphology from individual bubbles to the shape of the propagating crack. This crack develops similarly to fingering instabilities in Hele-Shaw cells filled with homogeneous fluids. We show that the observed width and shape of the crack are compatible this interpretation, and that the discreteness of the bubble structure provides symmetry perturbations and limiting scales characteristic of anomalous fingering. The model thus bridges the gap between fracture of the solid foam lattice and instability growth of interfaces in a fluid system.

1 Introduction

The analogue between the structure of a gas-liquid foam and the structure of a crystalline atomic solid (like metal) has long been established [1]. Apart from geometric analogies of defect motion and generation, as well as plasticity on the atomic scale [2, 3], recent research efforts have investigated how a qualitative understanding of fracture processes acting in a foam can illuminate the fracture morphology and dynamics in an atomic solid. In addition to such fundamental questions, the study of foam fracture is also of great relevance in applications relying on the integrity of liquid foams, e.g. in enhanced oil recovery [4], the manufacture of porous metallic solids [5], or in mineral flotation [6].

A prototypical system for the study of foam fracture has been developed both experimentally and in subsequent modeling efforts using a quasi-two-dimensional foam, *i.e.*, a single layer of bubbles between the parallel plates of a Hele-Shaw cell. The experimental realization of this concept has considered the phenomena upon injection of air into such a foam at a given pressure difference from one end to the other (open) end of the foam, while the bubbles are laterally confined to a rectangular region (see Fig. 1). Fracture is then observed to proceed along the direction of pressure drop in one of two distinct mechanisms depending on the rate of applied pressure. Much as in crystalline atomic solids, these mechanisms can be termed brittle and ductile: in the former case observed for large rates of applied pressure, very fast cleavages of the foam are sustained with very little deformation around the crack surface. These brittle cracks proceed by successive breakage of the thin films between foams in almost perfect sequence along the pressure gradient [7, 8]. In the latter case, observed for smaller rates of applied pressure, a much slower air/foam interface propagation is observed [9], morphologically resembling a fingering instability in homogeneous fluid systems described by Saffman and Taylor [10] and studied extensively as an example of nonlinear instability and shape selection [11–13]. While the system can also exhibit a brittle-to-ductile transition [8] between these modes, we will here focus on the ductile case only, see Fig. 1. A qualitatively

[*]School of Mathematics and Statistics, University of Glasgow, 15 University Gardens, Glasgow. G12 8QW UK
[†]Mechanical Sciences and Engineering, University of Illinois, Urbana-Champaign, IL

similar ductile foam invasion mechanism has also been observed in foams with a large bubble in the interior [14, 15], while fingering-type instabilities have been observed in foams where an interior bubble is continuously inflated [16, 17]. Experiments indicate that yield stress can significantly influence the fingering pattern in flowing polymer gels, but the effect of yield stress is notably absent in foams [18].

We have previously developed a large-scale network model to understand and quantify both modes of foam fracture under an applied driving pressure [19], based on a methodology developed for studying coalescence in molten metallic foams [20, 21]. This approach uses a simplified description of each of the fluid structures and incorporates an explicit film rupture criterion in the brittle case [22]. In the present study of ductile effects, the fast time scales of film rupture are unimportant, and the model focus lies on the (non-Newtonian) resistance of the foam bubbles when driven through the gap between the plates.

In this paper we utilize our network model to understand and quantify ductile fracture in large initially regular arrays, and connect our results to continuum theory of fingering in fluids. The model as it pertains to ductile fracture is briefly described in Sec. 2. It is then used to predict features of crack morphology and dynamics in Sec. 3, such as the mean crack width and crack tip speed as a function of the applied driving pressure. Finally, in Sec. 4 these numerical predictions are interpreted and compared to results on fingering in continuum fluid systems, including anomalous fingering in Newtonian fluids and shear thinning fluids. Sec. 5 provides conclusions and a discussion on the interrelation between fracture and fingering.

2 Ductile fracture model

We previously constructed a network model for foam fracture encompassing brittle and ductile effects [19] in a long Hele–Shaw cell of thickness (gap between the plates) b^* and lateral width W^*. In this study we use the same equations and notation with only small modifications which are detailed below. The domain is spanned by Cartesian coordinates, $\mathbf{x}^* = (x^*, y^*, z^*)$, where x^* is oriented across the channel width, y^* is in the direction of driving and z^* spans the Hele–Shaw cell thickness.

Throughout this study we focus attention on the ductile fracture mode and ignore the fast processes associated with film rupture (see [22] for details on film breakage in this setting). We denote ρ^* and μ^* as the density and dynamic viscosity of the water phase, respectively, and γ^* as surface-tension coefficient of the air-water interface (suitably modified by the presence of surfactants). We consider a regular hexagonal foam composed of bubbles of side length L with baseline pressure of the atmosphere P_0^*. The initial foam structure has appropriate modifications around the leading and trailing edges and along the side walls; see geometry in figure 2(a).

2.1 Variables and governing equations

The foam is subject to a driving pressure of ΔP applied to the leading edge, from which we construct a characteristic velocity scale $U_0 = (\Delta P/\rho^*)^{1/2}$. Lengths are scaled on L, velocities on U_0, time on L/U_0 and pressures are scaled according to

$$p^* = \Delta P\, p, \qquad P^* = \Delta P\, P, \tag{1}$$

where p (p^*) and P (P^*) are the dimensionless (dimensional) liquid and gas pressures, respectively. This results in a number of dimensionless groups,

$$\mathcal{R} = \frac{\rho^* U_0 L}{\mu^*}, \qquad P_0 = \frac{P_0^*}{\Delta P}, \qquad \gamma = \frac{\gamma^*}{\Delta P L}, \qquad b = \frac{b^*}{L}, \qquad W = \frac{W^*}{L}, \tag{2}$$

where $\mathcal{R}$ is the Reynolds number, P_0 is the dimensionless baseline gas pressure, γ is the surface tension coefficient, and b and W are the dimensionless Hele–Shaw cell thickness and width. The corresponding

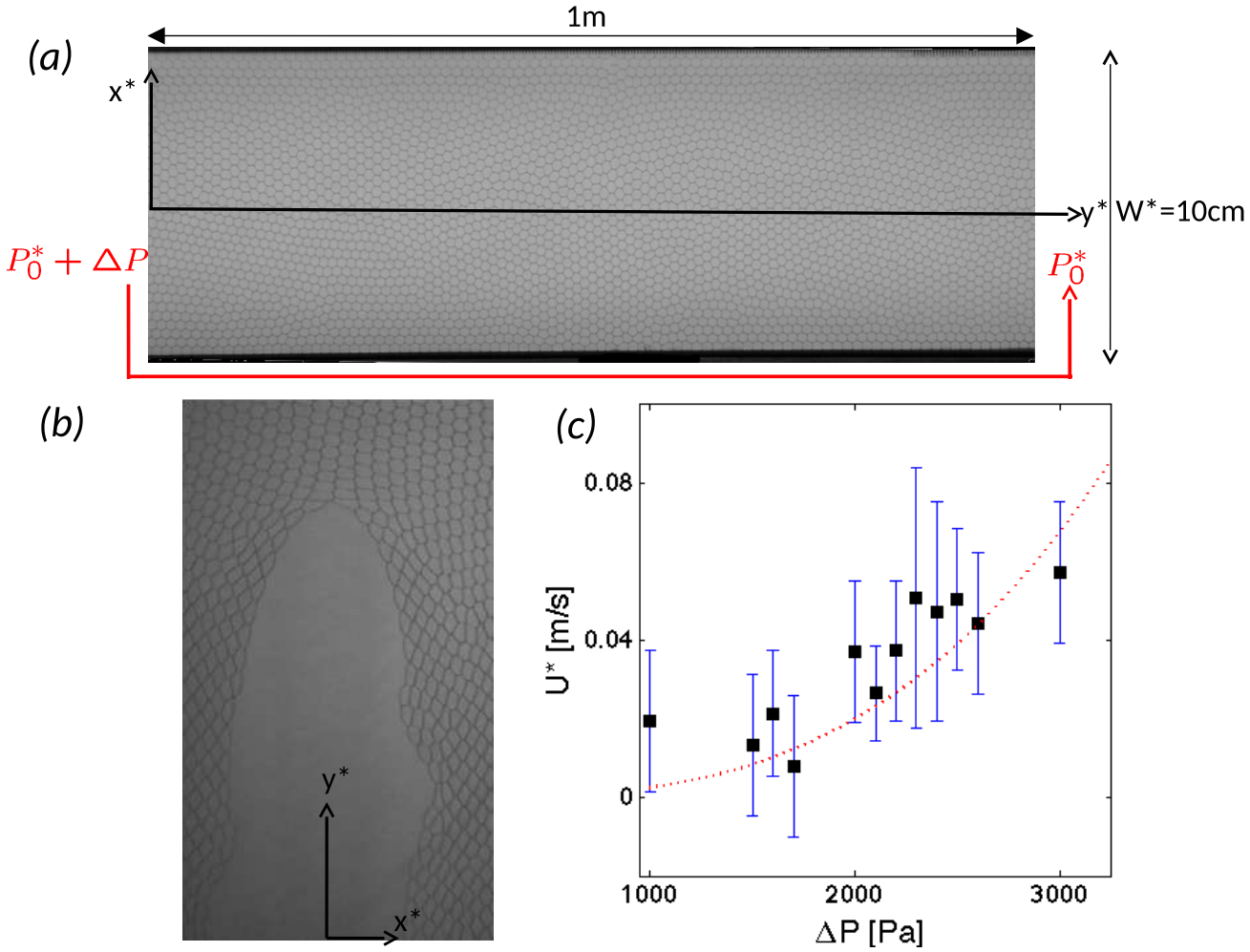

Figure 1: (a) Top view of a Hele-Shaw cell of width $W^* = 10\,\text{cm}$ and length $> 1\,\text{m}$ filled with a single layer of foam bubbles (edge length $L \approx 2\,\text{mm}$). A pressure difference is applied along the channel (y-direction) as indicated. (b) Typical experimental image of a propagating ductile crack (finger). The experimental field of view is limited to approximately the displayed length of the crack. The relative crack width determined from this image is at least $\overline{\lambda} \approx 0.39$. (c) Experimental data of ductile crack speed U^* vs. applied driving pressure ΔP (modified from [8]). The dashed line indicates the power law $U^* \propto \Delta P^{3/2}$, consistent with the modeling assumptions of the present work (cf. Eqn. (3b)).

dimensionless upstream and downstream pressures are denoted P_u and P_d, respectively. Here P_u is prescribed (detailed below), while $P_d = P_0$ throughout. In the experiments of Hilgenfeldt and coworkers the baseline pressure in the bubbles is atmospheric pressure, which is significantly greater than the applied driving pressure, so the dimensionless parameter $P_0 \gg 1$.

In network modeling of ductile fracture we neglect all out-of-plane motion and represent the foam by evolving the fluid structures on the plates, which we now consider in turn. A more complete description of each structure is given by [19].

Each Plateau border node (PBN) is modeled as a single point in space, denoted $\mathbf{x}_p$, moving in the plane of the plates with velocity $\mathbf{u}_p$, which are both functions of time, t. The PBN liquid structure on the plates is assumed to have uniformly curved gas-liquid interfaces with equal radii of curvature $\overline{a}_p$ in both directions (a sketch of the PBN geometry is given in figure 3 of [19]); $\overline{a}_p$ is assumed fixed for all

time. The equation of motion takes the form

$$\frac{\mathrm{d}\mathbf{x}_p}{\mathrm{d}t} = \mathbf{u}_p, \tag{3a}$$

$$\frac{\mathrm{d}}{\mathrm{d}t}\left(\frac{\overline{a}_p^3}{6\sqrt{2}}\mathbf{u}_p\right) = \sum_{m=1}^{3}\mathbf{F}_{pm} - \gamma^{1/3}\mathcal{R}^{-2/3}(3\overline{a}_p)K|\mathbf{u}_p|^{2/3}\hat{\mathbf{e}}_p, \tag{3b}$$

where $\hat{\mathbf{e}}_p$ is a unit vector in the direction of $\mathbf{u}_p$. On the right hand side of (3b), the first term represents the driving force on the node, while the second term represents the viscous resistance to motion across the fluid lining the plates; the form of the viscous drag term and the value of the numerical coefficient $K \approx 4.94$ follow from the calculation of [23] (based on Bretherton's classical analysis of closely fitting bubble in a capillary tube [24]) integrated around the perimeter of the PBN in contact with the plates (of length $3\overline{a}_p$). The nodal driving force $\mathbf{F}_{pm}$ $(m = 1, 2, 3)$ is proportional to the angle swept out between the two adjoining HPBs (in the plane of the plates) which we denote as $\phi_{m1} \le \phi \le \phi_{m2}$ $(m = 1, 2, 3)$ in the form

$$\mathbf{F}_{pm} = -\tfrac{2}{3}\overline{a}_p\gamma\left[\hat{\mathbf{x}}\sin\phi - \hat{\mathbf{y}}\cos\phi\right]_{\phi_{m1}}^{\phi_{m2}}, \qquad (m = 1, 2, 3), \tag{3c}$$

where $\hat{\mathbf{x}}$ and $\hat{\mathbf{y}}$ are unit vectors in the x and y directions, respectively. Experiments and simulations are conducted in the limit $\gamma \ll 1$, since the overall pressure difference greatly exceeds the Laplace–Young pressure. However, in ductile fracture the pressure drop between bubbles is significantly less than the overall pressure drop (as the pressure decreases linearly ahead of the crack tip, see figure 3(d) below), on the order of the Laplace–Young pressure or less, so we do not observe large deviations from a configuration where film angles $\phi_{m2} - \phi_{m1}$ are close to $2\pi/3$.

In the ductile regime each horizontal Plateau border (HPB) is modelled as a uniformly curved line in the plane of the plates connecting adjacent PBNs; HPB curvature $\kappa_h(t)$ is determined using a Laplace–Young balance in the form

$$[P]_-^+ = 2\gamma\kappa_h, \tag{4}$$

where $[P]_-^+$ denotes the jump in gas pressure across the two free surfaces of the HPB, which is balanced by the restoring influence of surface tension.

Finally, the pressure P_j in gas bubble j of current volume V_j follows from an isothermal equation of state in the form

$$P_j V_j = P_0 V_{j0}, \tag{5}$$

where V_{j0} is the initial volume of bubble j.

The numerical calculation proceeds using solver `ode15s` in MATLAB by explicitly calculating the positions of the PBNs (which follow from Eqn. (3)) and the positions of the HPB midpoints (which must be chosen to satisfy Eqn. (4)) at each timestep. So at any given step the HPB curvature and, hence, the total bubble volume can be easily computed; the corresponding bubble pressure then follows from (5).

2.2 T1 transitions and discrete effects

In ductile fracture the crack tip advances not by film rupture, but through bubbles interchanging their neighbours through successive T1 transitions. In this network model formalism these transitions occur when any two nodes come within a distance of $2\overline{a}_p$, where we enforce a neighbour interchange in the same way as previous vertex models [25], described in more detail in [20]. Note that the presence of discrete T1 transitions means that not only is the instantaneous shape of the crack outline 'grainy' on the bubble scale, but also the dynamics of its propagation is punctuated by discrete events. Thus, the morphology of ductile foam fracture is necessarily fluctuating in space and time. This can be appreciated in Fig. 4 below, where subsequent crack shapes are shown around a particular T1 transition. The shape of the tip is distorted noticeably in the course of the event.

Due to limitations of CPU time effort, the simulations presented here were made for a foam about 15 bubbles across its width (x-direction). Effects of discrete bubble rearrangements are therefore fairly strong on the scale of the entire crack outline.

2.3 Computing the elastic stress

Another consequence of the discreteness of the bubble structure is a certain degree of heterogeneity in mechanical stress. It is simple to compute the maximal deviatoric stress exerted on each gas bubble in the foam as

$$\overline{S^j} = \sqrt{-\det(\mathbf{S}^j)} \geq 0\,, \tag{6}$$

where the deviatoric stress tensor is given by

$$\mathbf{S}^j = \mathbf{\Sigma}^j - \tfrac{1}{2}\mathrm{Tr}(\mathbf{\Sigma}^j), \tag{7}$$

computed based on the microscopic stress tensor for bubble j, denoted $\mathbf{\Sigma}^j$. The stress tensor $\mathbf{\Sigma}^j$ is approximated following an approach developed for granular materials [26]. For a given bubble, each constituent PBN experiences a surface tension force from the attached film that does not form part of the bubble outline; the components of the microscopic stress tensor can be found by summing the moments of these forces about the centre of the bubble. Further details are given in [19]. The principal stresses and their directions are then computed as the eigenvalues and eigenvectors of the deviatoric stress tensor $\mathbf{S}^j$. In figure 2 below we illustrate several snapshots of the stress profile in a typical example using a colour map of the maximal stress per bubble and further illustrate the direction of the principal stresses using a cross centred in each bubble. While there is a great degree of order on the scale of the length of the foam, illustrating the expected linear pressure profile in front of the crack tip, the deviatoric stresses show strong variations around the crack interface – the stress is concentrated in lobes around the tip, but cannot be said to have a smooth distribution resembling what is computed in continuum fracture theory [27].

2.4 Describing the crack shape and dynamics

From the numerical simulations, we now extract macroscopic parameters describing the shape and dynamics of the propagating crack. For a given simulation we estimate the position of the tip of the crack in the laboratory frame as the y-position of the most advanced node on the leading edge of the foam, denoted $y = y_f(t)$. We then compute the corresponding length of the crack L_c by subtracting the y-position of the rearmost node on the leading edge. The estimated crack tip position y_f and crack length L_c are shown for the example in figure 3(a) below. In simulations reported below we sample the crack tip position every two dimensionless time units over a chosen interval and then fit a straight line through these points; the gradient of this line is the corresponding speed of propagation.

The width of the crack at any time denoted $w(t)$ is estimated by computing the current area encompassed by the crack (the polygonal shape encompassed by the nodes on the crack interface) and dividing by the maximal length of the crack L_c. For a typical example the crack area is highlighted in figure 3(a) below. In the analysis of the data, we will concentrate on the crack width relative to the channel width, denoted $\lambda(t) = w(t)/W$.

To estimate the curvature of the crack tip we isolate the three PBNs closest to the crack tip and compute the parabola $y_c(x)$ which passes through these three points. The instantaneous radius of curvature of the crack tip, denoted $\rho(t)$, is then obtained by computing the curvature of this parabola at its maximal value. Two typical examples are shown as dashed lines in figure 3(a,b) below. This technique of determining tip curvature by fitting a parabola has been used extensively in experiments and computations of fingering in continuum fluids [11, 13].

2.5 Setup of numerical simulations

For numerical simulations we construct an initially regular hexagonal configuration similar to (but considerably larger than) those described in [19], composed of approximately 400 bubbles with a dimensionless width of $W = 22$. Reflecting a typical experimental geometry [7, 9], we set $b = 1/2$, so that the aspect ratio of the channel cross-section is $W/b = 44$.

A symmetric notch is created on the leading edge by rupturing a single film in the centre of the domain. However, such a geometry introduces an artificial bilateral symmetry around the y-axis not compatible with the stochastic nature of T1 events in experiments. To break the symmetry we inflate one bubble to the right of the notch in the interior of the foam (marked in Fig. 2(a)) by increasing its initial volume by 20%, and allow the system to reach a new equilibrium. A typical initial configuration is shown in Fig. 2(a).

In [19] the driving pressure was ramped linearly over the interval $t = [0, t_R]$ to a value ΔP_d and then held constant, reflecting experimental protocols. According to our non-dimensionalisation (1), this total driving pressure difference should be set to 1 dimensionless unit. However, since our foams are much shorter relative to the bubble size than the experiments of [9], to achieve a comparable pressure drop per bubble we instead consider $0 \leq \Delta P_d \leq 1$.

In [19] the driving pressure is held constant beyond $t \geq t_R$; as the length of foam ahead of the crack tip becomes shorter so the relative driving pressure per bubble increases and the crack accelerates. This feature is not evident in the experiments, where the domains are much larger – when the linear pressure gradient in front of the crack tip has developed, its value does not change appreciably over the field of view in experiment, and thus a steady propagation is recorded. To overcome this issue, and allow the crack to reach an approximately steady propagation speed, we adjust the driving pressure as the corresponding length of foam ahead of the crack tip reduces.

We compute the length of the foam ahead of the crack tip, denoted $\mathcal{L}(t)$, by subtracting y_f from the largest y-coordinate of PBNs on the trailing edge. Denoting $\overline{\Delta P_d}$ as the maximal applied pressure drop (at $t = t_R$), we compute the corresponding pressure drop per unit length of foam ahead of the crack as $P_l = \overline{\Delta P_d}/\mathcal{L}(t_R)$. To ensure that P_l is held approximately constant, at fixed time intervals of 2 (dimensionless) units we reduce the driving pressure ΔP_d to reset $P_l = \Delta P_d/\mathcal{L}$ to its target value, so $\Delta P_d = \overline{\Delta P_d}\,(\mathcal{L}(t)/\mathcal{L}(t_R))$.

The ramping protocol for the upstream driving pressure thus takes the form

$$P_u(t) = P_0 + \overline{\Delta P_d} \times (t/t_R), \qquad (0 \leq t \leq t_R)\,, \tag{8a}$$

$$P_u(t) = P_0 + \Delta P_d(t), \qquad (t > t_R)\,. \tag{8b}$$

A typical plot of P_u against time is shown in Fig. 2(e) below. In all simulations described below we set $t_R = 100$, as in [19]. In the present study the range is $0.2 \leq \overline{\Delta P_d} \leq 0.35$. Note that in ductile fracture the important feature for the modeling is to quantify the balance of driving and resistance on each bubble. For values of $\overline{\Delta P_d}$ larger than this range we observe tip splitting (as observed in continuum fluids for large finger velocities [28]). Conversely, for $\overline{\Delta P_d}$ smaller than this range the computation time for the simulations become prohibitively expensive.

3 Results for ductile fracture

3.1 Baseline example

As a baseline example in Fig. 2 we illustrate four snapshots of ductile fracture for $\overline{\Delta P_d} = 0.3$ in a foam initially composed of ≈ 400 bubbles. In panels (a)-(d) we illustrate the outline of each gas bubble formed by PBNs at the vertices (filled black circles) connected by HPBs (black lines). Furthermore, in Fig. 2(a-c) we illustrate the maximal stress per bubble as a colormap and highlight the magnitude and direction of

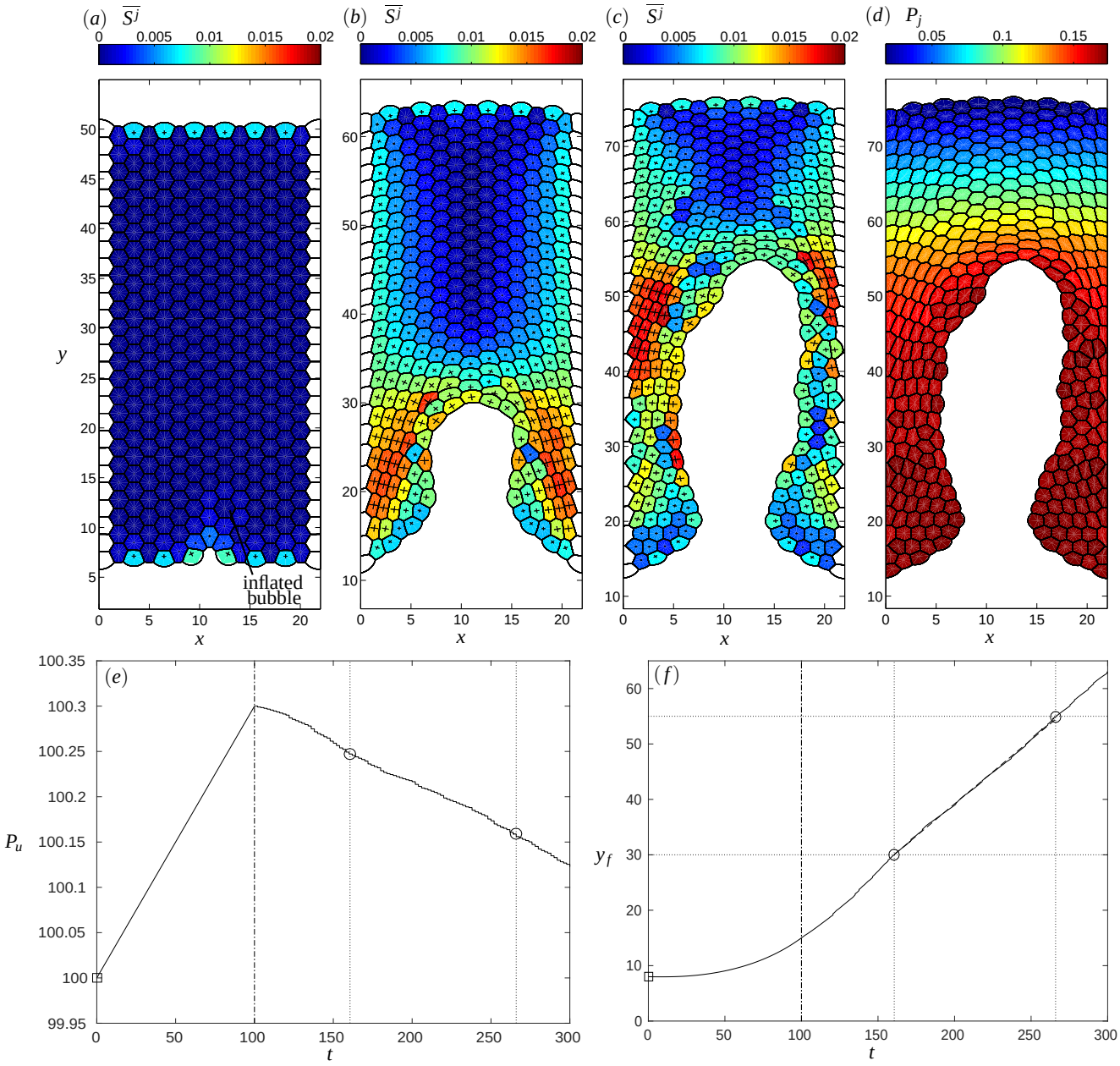

Figure 2: Snapshots of a typical ductile crack for $\overline{\Delta P_d} = 0.30$ for $t_R = 100$ showing a colormap of the maximal deviatoric stress in each interior bubble at three time points: (a) $t = 0$; (b) $t = 160.6$ when $y_f \approx 30$; (c) $t = 266.0$ when $y_f \approx 55$. The cross in each interior bubble illustrates the principal directions of deviatoric stress. Panel (d) shows the gas pressure distribution corresponding to panel (c) at $t = 266.0$. For this simulation we also plot the temporal evolution of: (e) the applied driving pressure P_u; (f) the crack tip position y_f. The bubble labelled in (a) is inflated by 20% to introduce an asymmetry in the resulting ductile crack propagation. Here $\gamma = 0.0125$, $\mathcal{R} = 2000$, $K = 4.94$, $\overline{a}_p = 0.2$, $P_0 = 100$.

principal stress in each bubble as a cross in each bubble. A movie of the evolution of the maximal stress during this ductile fracture example is provided as online supplementary material. Conversely in Fig. 2(d) we illustrate the gas pressure at the same time instant as reported in Fig. 2(c) where, as expected, the

pressure profile ahead of the crack tip decreases linearly in y [19]. In Fig. 2(e) we illustrate the applied driving pressure P_u to maintain a constant pressure drop per bubble for $t \geq t_R$, decreasing stepwise every 2 dimensionless time units, while in Fig. 2(f) we show the change in the position of the crack tip $y_f(t)$. Following ramping, we isolate a spatial interval where we have steady state propagation of a ductile crack at a well-defined velocity with a well-defined shape. In this example, and in those considered below, we use the interval $30 \leq y_f \leq 55$ where we construct a line of best fit (shown as a dashed line in Fig. 2f) with gradient $U \approx 0.2315$. For the example in Fig. 2 we have 145 T1 transitions in this interval. In App. A we show that a range of intervals in y_f can be chosen without affecting the conclusions of the present work.

The dynamics of ductile fracture are qualitatively similar to that already described in [19]. We stress here that under the conditions employed here (constant pressure drop per bubble), the crack reaches a steady state with well-defined, constant propagation speed U and constant relative width λ. The crack tip advances through successive T1 transitions in a 'plasticity' zone around the crack tip, which enables bubbles to be displaced to the sides of the advancing crack; while this causes fluctuations in the crack speed and width, its overall dynamics and shape is that of a macroscopic finger analogous to that observed in Saffman-Taylor experiments. A more detailed comparison of the shape of these fingers is made in Sec. 4 below.

In order to describe the morphology of the crack in more detail, in Fig. 3 we consider the crack tip radius of curvature and the corresponding relative crack width. In particular, we illustrate the outline of the leading edge of the crack (solid line with filled black circles at nodes) at two selected time intervals $t = 160.0$ (Fig. 3a, see also Fig. 2b) and $t = 266.0$ (Fig. 3b, see also Fig. 2c,d). The shaded area in Fig. 3(a) highlights the crack area (used in estimating the crack width), while the dot-dashed line represents the measured crack length. The fitted parabola through the three furthermost advanced nodes, used to estimate the radius of curvature of the crack tip, is shown as the dashed line in both panels. We notice that even though the parabola is only fitted using three points, it passes very close to a number of other nodes on the crack tip. In addition, the crack adopts an approximately constant width along its length, similar to fluid fingering (as discussed in Sec. 4 below). In Fig. 3 we further consider the temporal change in the crack morphology, showing the evolution of the crack tip radius of curvature $\rho(t)$ (Fig. 3c) and the relative crack width $\lambda(t)$ (Fig. 3d) over the course of the baseline simulation. The computed crack tip radius of curvature (which has been smoothed using a five point moving average, Fig. 3c) increases as the crack develops, but fluctuates with large amplitude at later times due to changes in morphology induced by T1 transitions on the crack tip (see Fig. 4 below). Conversely, the relative crack width initially increases as the crack develops but saturates to an approximately constant value that is relatively unaffected by T1 transitions (Fig. 3d). The transient increase (or overshoot) in crack width is a consequence of the way the crack develops from the initial notch in the geometry. Beyond this initial transient the crack width is less than half the width of the channel ($\lambda < 1/2$), consistent with observations of fingering in non-Newtonian fluids [13].

To understand the large fluctuations in crack tip radius of curvature evident in Fig. 3(c), in Fig. 4 we illustrate the change in morphology through a particular T1 transition at $t \approx 200.765$, showing snapshots of the foam and the corresponding deviatoric stress distribution shortly before ($t = 200.0$, Fig. 4a) and after ($t = 202.0$, Fig. 4b) the event. This T1 event results in a sharpening of the crack tip and hence a sharp decrease in the radius of curvature (significant change in the fitted parabola, shown as a dashed line in both panels), evident in Fig. 3(c) for $t \approx 200$. Such changes are to be expected given the discrete make-up of the crack tip of individual bubbles, so that relatively large changes in crack tip radius of curvature can be observed without showing much overall morphological change.

3.2 Simulations for a range of driving pressures

To assess how the properties of the crack propagation change as we adjust pressure driving, in Fig. 5 we summarise simulations across maximal applied driving pressures in the range $0.2 \leq \overline{\Delta P_d} \leq 0.35$. In

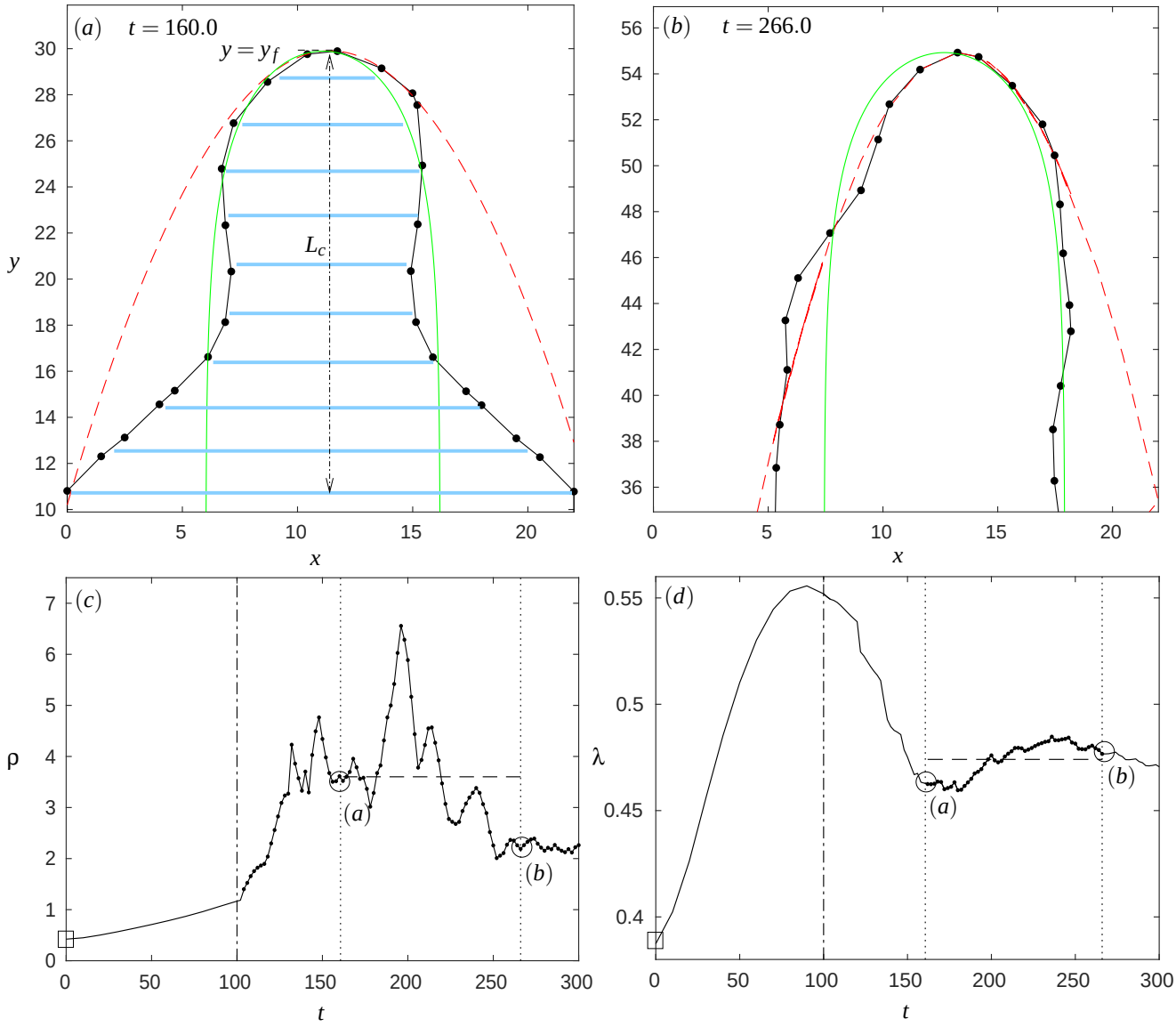

Figure 3: The outline of the leading edge of the crack at two fixed time intervals for $\overline{\Delta P_d} = 0.30$ and $t_R = 100$ as shown in Fig. 2: (a) $t = 160$ (close to panel (b) in Fig. 2) (b) $t = 266$ (close to panel (c) in Fig. 2). The dashed red lines in represent the fitted parabolae through the three most advanced points on the crack tip from which the radius of curvature is computed, while the shaded area represents the crack area and the dot-dashed line the crack length. The green line represents the corresponding prediction of the anomalous finger shape (9). Also shown are the temporal evolution of: (c) radius of curvature of the crack tip $\rho(t)$ sampled every two time units and smoothed using a five point moving average; (d) relative crack width $\lambda(t)$.

particular, across this range of $\overline{\Delta P_d}$ we quantify the variation in the time of the first T1 transition t_1 (Fig. 5a), the measured crack speed in the steady state U (Fig. 5b), the corresponding mean crack width $\overline{\lambda}$ (Fig. 5c) along with the mean crack tip radius of curvature $\overline{\rho}$ (Fig. 5d) fitted using the procedure outlined above. It should be noted that U, $\overline{\lambda}$ and $\overline{\rho}$ are sampled from the interval $30 \leq y_f \leq 55$, where the crack is (approximately) propagating steadily.

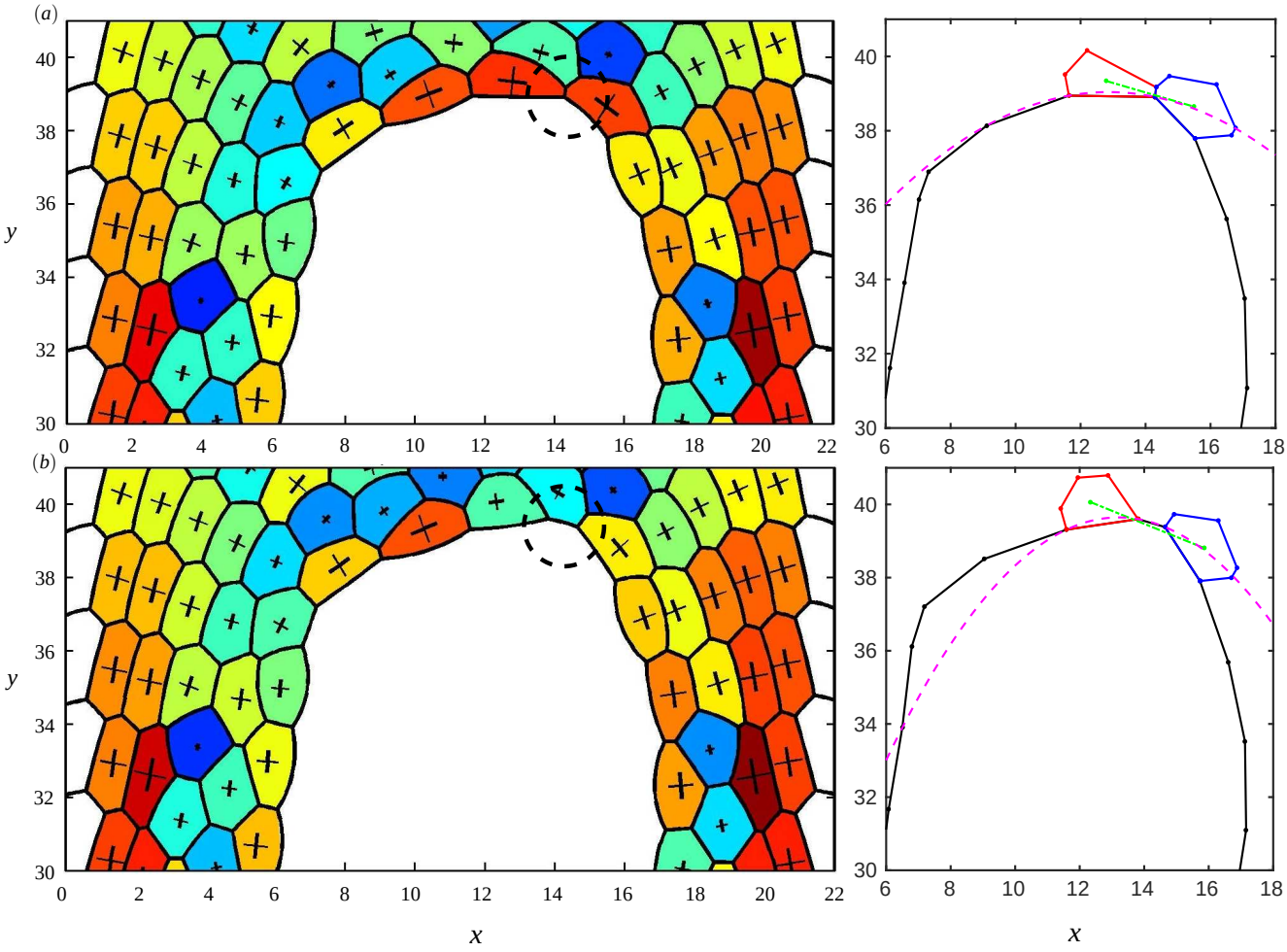

Figure 4: The stress distribution around the crack tip for the baseline simulation shown in Fig. 2 showing the distortion in the shape of the crack tip in the course of the T1 event: (a) $t = 200.0$; (b) $t = 202.0$. In both cases the panel to the right shows the crack outline (solid line with filled black circles) along with the polygonal outline of the bubbles that undergo T1 transition. The dashed line represents the fitted radius of curvature through the crack tip and the dot-dashed line represents the distance between the two bubble centers.

As might be expected, it emerges that the time of the first T1 transition decreases markedly as the pressure ramping is increased (Fig. 5a) while the corresponding crack tip speed broadly increases as a function of the driving pressure, although there is some small variation, following the trend of a power law $U \propto \overline{\Delta P_d}^{3/2}$ shown as a dashed line (Fig. 5b) consistent with the Bretherton [24] prediction, used in constructing the viscous drag in (3b). However, in the present case the range of $\overline{\Delta P_d}$ is very small, so other functions might also fit reasonably well. By contrast, the morphological parameters describing the width and curvature of the crack show no significant change over the simulation range. The crack width is always less than $\lambda = 0.5$ (the classical value for a Saffman-Taylor (ST) finger between Newtonian fluids), consistent with the cracks seen in the experiments (see Fig. 1) while the mean crack tip radius hovers around $\bar{\rho} \approx 2 - 3$. We find, therefore, that the fingers have a well-defined continuum shape, but that it differs from the ST solution. This could have been expected, as detailed investigations of viscous fingering have shown that the ST solution is replaced by different finger shapes when its symmetry is perturbed [11, 29] or when the fluid media in the Hele-Shaw cell are non-Newtonian [13, 18].

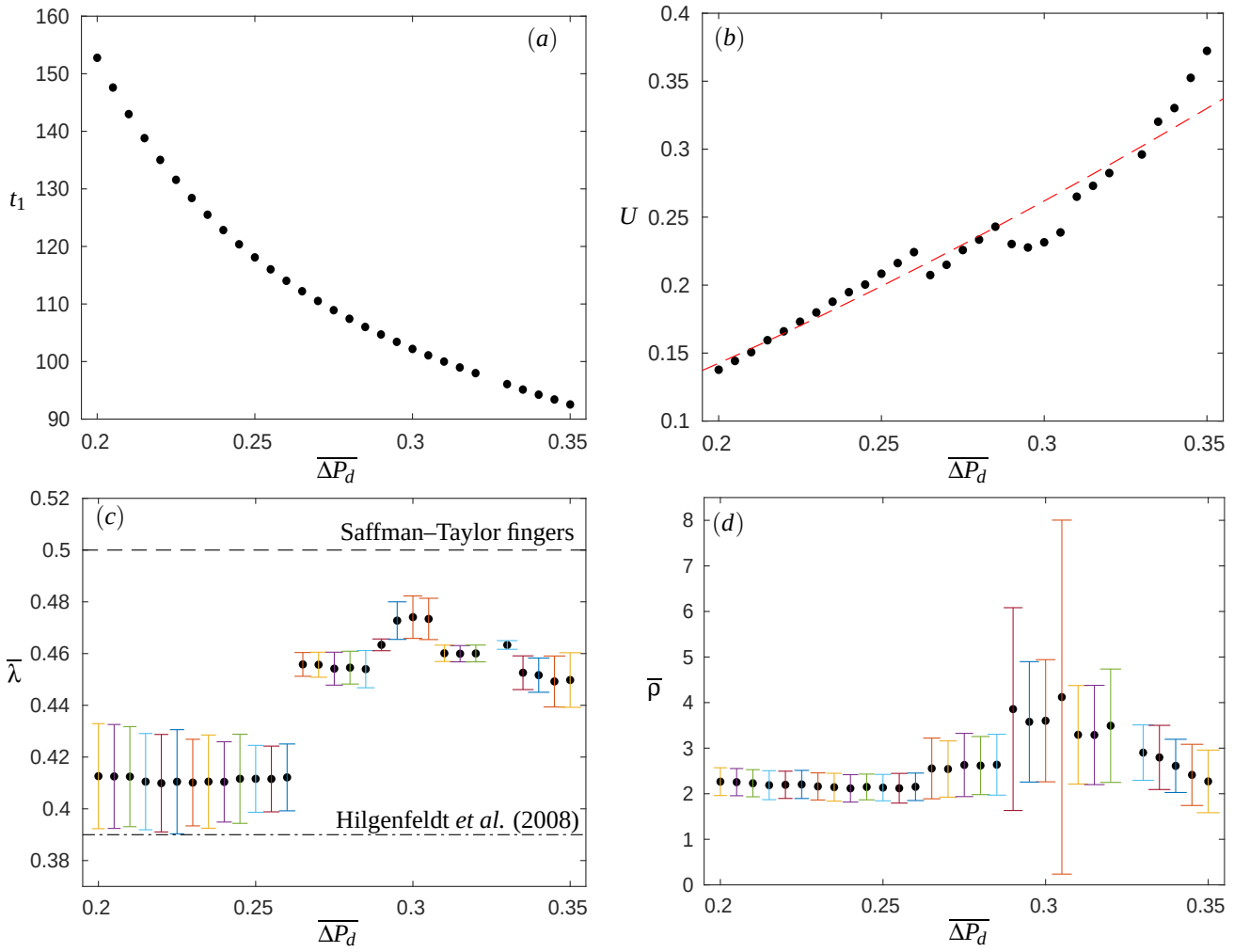

Figure 5: Filled black circles illustrate summary results from 30 simulations of ductile fracture for driving pressures in the range $0.20 \leq \overline{\Delta P_d} \leq 0.35$ sampled at intervals of 0.005 (all other parameters identical to the case considered in Fig. 2): (a) time taken for the first T1 transition. In addition, we illustrate the mean properties of the crack tip while in the interval $30 \leq y_f \leq 55$ showing: (b) computed crack tip speed; (c) mean (relative) crack width; (d) mean crack tip radius of curvature over the interval. The dashed line in (b) represents the power law $U \propto \overline{\Delta P_d}^{3/2}$ comparable to the experimental observations (see Fig. 1).

In Fig. 5 we observe that for low $\overline{\Delta P_d}$ the values of $\overline{\rho}$ and $\overline{\lambda}$ are remarkably consistent (in the range $\overline{\Delta P_d} = 0.2$ to $\overline{\Delta P_d} = 0.26$). The morphology of the crack in this range is summarised in Fig. 6, showing a typical outline of the crack (Fig. 6a) and the temporal evolution in the crack tip radius of curvature (Fig. 6b). Across the simulations the crack shape is essentially constant, lengthening at a uniform rate (and compares very well with shapes in viscous fingering discussed below). A small but significant change in crack morphology is evident around a driving pressure of $\overline{\Delta P_d} = 0.26$; possible reasons for this transition are discussed in Sec. 4 and App. A below.

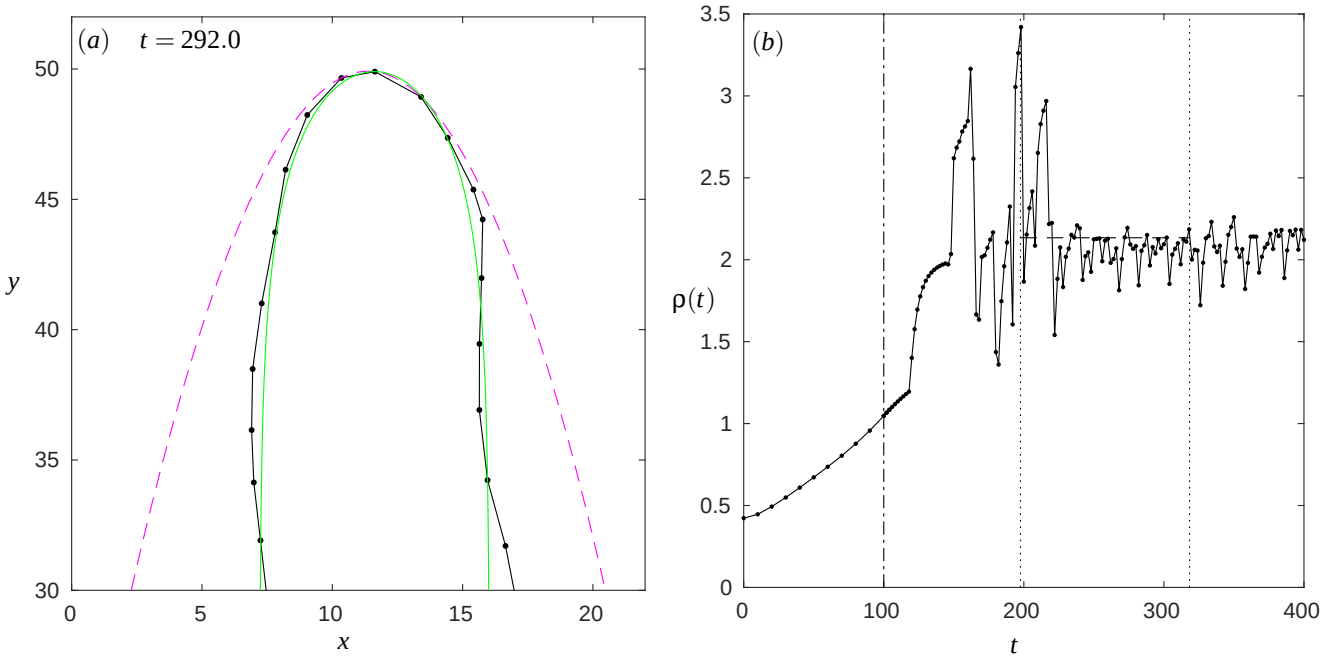

Figure 6: Summary of simulations with $\overline{\Delta P_d} = 0.25$ for all other parameters identical to Fig. 2, showing: (a) the outline of the crack tip for $t = 292.0$ with filled black circles joined by solid lines; (b) the temporal evolution of the computed crack tip radius of curvature sampled every two time units and smoothed using a five point moving average. The dashed line in (a) is the parabolic fit through the crack tip, while the solid green line is the corresponding anomalous finger shape (9). In (b) the interval of steady propagation between $30 \leq y_f \leq 55$ is enclosed between the dotted lines.

4 Comparison to fluid fingering

4.1 Anomalous fingering in Newtonian fluids

The classical ST solution of a single symmetric finger with $\lambda = 1/2$ (at large capillary number $C = \tilde{\mu}^* U^*/\gamma^*$, for a viscosity $\tilde{\mu}^*$ of the invaded fluid with dimensional finger tip speed U^*) has been explained [30] by a singular perturbation selection mechanism. The flow between the plates is modeled in the spirit of a Hele-Shaw flow (a two-dimensional flow averaged across the z-axis), obtaining explicit solutions for the motion of the invading fluid (of lower viscosity), the invaded fluid (of larger viscosity), and the interface shape. While the ST scenario of a less viscous fluid invading a more viscous one in a rectangular channel initially appears to allow for a continuum of solutions of the shape (using our notation with finger tip at $(x, y) = (x_f, y_f)$)

$$y_s(x) = y_f + \frac{W(1-\lambda)}{2\pi} \ln\left[\frac{1}{2}\left(1 + \cos\left(\frac{2\pi(x - x_f)}{\lambda W}\right)\right)\right], \tag{9}$$

the presence of even infinitesimal surface tension leads to the selection of discrete values of λ consistent with the symmetry of the finger around $x = x_f$ [10, 30].

Of those solutions, only the widest finger, with $\lambda = 1/2$, is stable. However, it was shown experimentally [11, 29] and theoretically [31] that a perturbation of the symmetry by means of grooves in the plates, wires strung parallel to the channel, or small bubbles ahead of the finger tip, leads to a breakdown of the ST selection criterion, and the continuum of solutions (9) for the finger width becomes possible again. Such fingers have been termed 'anomalous' [32], although they are probably more commonly encountered

in experiments not carefully tuned to show ST selection. The morphology of anomalous fingers closely obeys (9), while the realized λ depends on C, decreasing as $C \to \infty$.

Rabaud *et al.* [11] showed that the finger width also scales with the aspect ratio W/b of the Hele-Shaw cell, so that all widths can be plotted against the universal parameter $1/B \equiv 12C(W/b)^2$, resulting in

$$\lambda(1/B) = \frac{\pi\alpha\sqrt{B}}{2}\left[\left(1+\frac{4}{\pi\alpha\sqrt{B}}\right)^{1/2} - 1\right], \tag{10}$$

where α is a constant parameter specific to the case of anomalous fingering.

This formula predicts arbitrarily sharp fingers (with curvature $\rho \to 0$ at the tip) as $1/B \to \infty$. However, experimentally these anomalous fingers asymptote to a finite minimal width λ_m when the radius of curvature approaches $\rho_m = \beta b$, with $\beta \approx 2.2 - 2.5$ [29]. This is interpreted as the limit of describing the system as an essentially two-dimensional continuum: the Hele-Shaw approximation breaks down, and the shape of the tip of the finger becomes determined by the full three-dimensional shape of the interface between the fluids. We will show below how the discrete structure of the foam provides a mechanism for both anomalous finger propagation and a saturation of the finger width.

4.2 Anomalous fingering in shear-thinning fluids

As gas-liquid foams are commonly modelled as continuum fluids with a non-Newtonian (shear thinning) rheology [33], it is instructive to compare our case with fingering in non-Newtonian continuum fluids. In the study of Lindner et al. [13], fluids were considered whose rheology is approximately that of a shear-thinning power-law fluid with exponents in the range $n \approx 0.25$ to $n \approx 0.75$, i.e., where the (dimensional) shear stress τ^* is related to the (dimensional) shear rate $\dot{\epsilon}^*$ by

$$\tau^* = k_1(\dot{\epsilon}^*)^n, \tag{11}$$

where k_1 is a constant. Experimentally, this was realized by xanthane solutions of various concentrations. When a Saffman-Taylor fingering experiment was set up using air to invade these fluids, the results closely resembled anomalous fingering: the finger width decreased below $\lambda = 1/2$ for increasing $1/B$ following (10) with α depending on n, and eventually saturated at a finite value. However, in this case (i) the radius of curvature at the tip was considerably larger than in the Newtonian case ($\rho/b \gtrsim 13$), and (ii) the finger width tended to increase as $1/B$ was increased further beyond the point of apparent saturation. While no unambiguous physical explanation was offered for these findings, it is clear that shear-thinning fluids sustain anomalous fingers. Similar conclusions were also drawn in theoretical work for shear-thinning fluid fingering [12], although no direct comparison to experiment was attempted. Does our network model of foam, without any imposed continuum properties, give rise to similar behavior?

4.3 Anomalous fingering in foams

As a first comparison between our ductile fractures and anomalous fingers, for $\overline{\Delta P_d} = 0.3$ in Fig. 3(a,b) we superimpose the corresponding anomalous finger shape (9) for the instantaneous crack width λ and crack tip position $(x, y) = (x_f, y_f)$ where x_f has been fitted to the 20 most advanced nodes on the crack tip. In this case the discreteness of the crack outline and the transient nature of the crack tip radius of curvature induces significant differences in comparison to the continuum profile (especially in Fig. 3b). However, superimposing the corresponding anomalous finger shape (9) for $\overline{\Delta P_d} = 0.25$ in Fig. 6(a), we see much closer agreement with the network model predictions.

The rheological behavior of the quasi-2D foam is implicit in our model: equation (3b) is a dimensionless balance between the driving force on the nodes and the viscous resistance on the plates of the Hele-Shaw cell, in the spirit of Bretherton's classical work [19,24]. Interpreted as a continuum medium, this equates to a shear-thinning fluid with an exponent $n = 2/3$.

For the purpose of describing an effective foam rheology at the crack tip, we now determine an effective averaged shear stress: Each bubble on average contains six nodes and each node is shared between three bubbles, so that the total viscous force from the two nodes per bubble is twice the final term in (3b)). Dividing by the area of a regular hexagonal bubble yields a (dimensionless) average shear stress,

$$\tau = \frac{4}{3\sqrt{3}}(3\overline{a}_p)\gamma^{1/3}\mathcal{R}^{-2/3}K|U|^{2/3}\,. \tag{12}$$

An effective dimensional shear viscosity for the foam can then be defined as

$$\tilde{\mu}^* = \tau^*/\dot{\epsilon^*} \tag{13}$$

where $\dot{\epsilon^*}$ is a shear rate and our non-dimensionalisation implies that $\tau^* = (\Delta P)\tau$. This effective viscosity $\tilde{\mu}^*$ is an important parameter for bridging the gap to continuum modeling, as it defines an effective capillary number $C = \tilde{\mu}^* U^*/\gamma^*$, where the dimensional crack tip velocity follows from $U^* = U_0 U$. For this purpose, $\dot{\epsilon^*}$ has to be estimated as an average (absolute value of the) shear rate between the plates. The foam bubble flow strongly resembles a plug flow, so that the relation to the tip velocity is $\dot{\epsilon^*} \approx 2U^*/b^*$.

We remark that the range of capillary numbers obtained for our simulations in this fashion (using the bubble size, surface tension, and other parameters of [8]) is $C \approx 0.017$ to 0.035. If we instead estimate the capillary number using the general foam rheology equations obtained in Denkov *et al.* [34] with a 2/3 power law, for our simulations we obtain a range $C \approx 0.05$ to 0.097, within a factor of three. This reasonable agreement supports the self-consistency of our approach. From the established effective capillary number, we compute the control parameter for the selection of finger width $1/B = 12C(W/b)^2$.

This interpretation of the foam as an effective power law medium without yield stress between the plates is consistent with the observations of Lindner *et al.* [18]. Note that the foam still possesses a yield stress in the $x-y$ plane that needs to be overcome for T1 transitions to take place. Following, [35], this yield stress can be estimated as $\sim 0.4\gamma^*/L \approx 5$Pa for our parameter values. Multiplying this value by a film area estimates a tangential force necessary to effect T1s; indeed, the force obtained from integrating (12) over the area of one bubble is comparable (and usually somewhat larger) than this estimate, so that the model's T1 transitions are consistently represented in dynamical terms.

Following Rabaud *et al.* [11], an analytical prediction for the radius of curvature at the tip of the steadily propagating finger as a function of the relative crack width λ is

$$\rho = \frac{\lambda^2 W}{\pi(1-\lambda)}. \tag{14}$$

The predictions of this equation can be compared directly to the results of our numerical simulations in Fig. 7(a). Note that we have chosen the evaluation of ρ from local PBN positions at the tip in order to make this comparison meaningful; (14) explicitly refers to the curvature at the tip only. For slower driving $0.2 \leq \overline{\Delta P}_d \leq 0.26$ the computed points (shown as filled circles) cluster together close to the prediction (14) and show very good agreement, so our discrete simulations accurately reproduce the continuum finger shapes. However, for $\overline{\Delta P}_d > 0.26$ the computational results (shown as open circles) are more scattered around the theoretical curve as it takes much longer for the foam to settle into a consistent pattern. This feature is explored further in Appendix A, where we show that the degree of scatter is approximately independent of the spatial interval over which the mean tip radius of curvature and crack width are sampled (see Fig. 8b). Overall, the applicability of (14), and values of $\lambda < 1/2$, suggest that the shape of our ductile cracks is well-approximated by that of anomalous fingers.

The finger width, however, does not show a pronounced dependence on the driving parameter $1/B$ as determined above (Fig. 7b), even though over the range of driving pressures the crack speed varies by a factor of about three (Fig. 5b). In the context of anomalous fingering, this could be explained if the finger width has saturated to a minimum value λ_m. In Fig. 7(b) we also plot the function (10) as

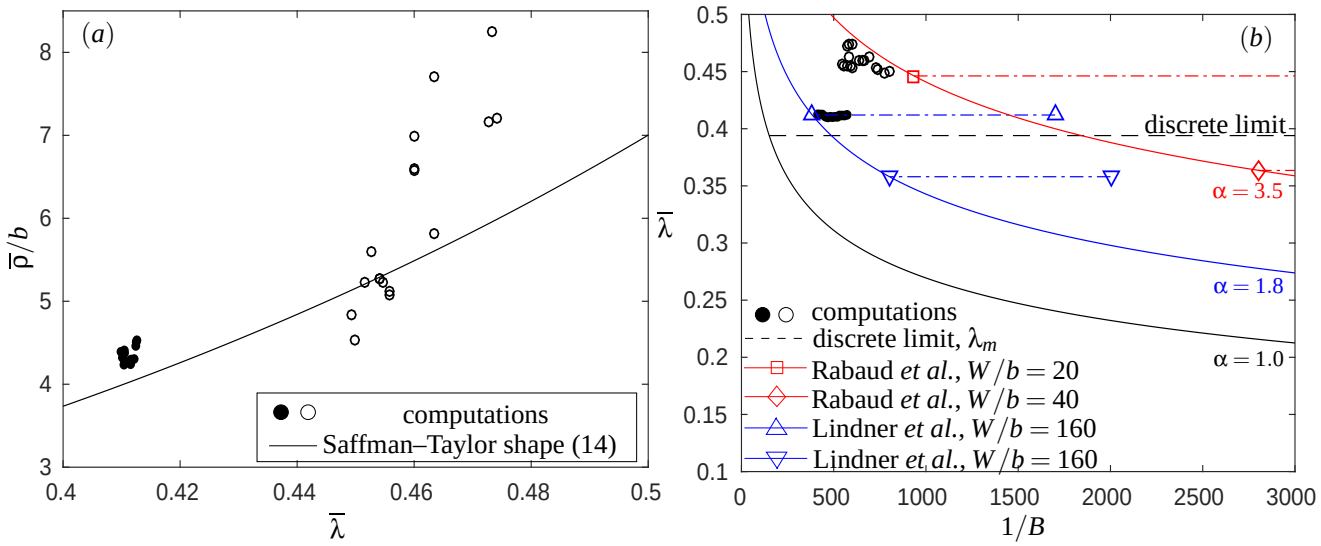

Figure 7: Comparison of the numerical predictions summarised in Fig. 5 to studies of fingering in continuous media showing (a) the crack tip radius of curvature as a function of the relative crack width constructed from the network simulations (circles – filled for $\overline{\Delta P_d} \leq 0.26$, open for $\overline{\Delta P_d} > 0.26$), compared to the asymptotic result for Saffman–Taylor fingers (14); (b) the relative crack width constructed from the network model simulations as a function of the dimensionless parameter $1/B$ (symbols as in (a)). For comparison, we indicate literature results from anomalous fingering as the expected $\bar{\lambda}(1/B)$ function (10) for various values of α (solid lines) as well as the saturated widths λ_m (dot-dashed lines) reported in Newtonian fluid experiments [11] for $W/b = 20$ (dot-dashed line with open squares) and $W/b = 40$ (dot-dashed line with open diamonds), and for shear-thinning fluid experiments [13] for $W/b = 160$ (dot-dashed lines with open triangles). The discrete limit λ_m is shown as a dashed line.

the solid lines, for values of $\alpha = 1.0$ (black), $\alpha = 1.8$ (blue), and $\alpha = 3.5$ (red). This is a typical range of α in previous studies, and $\alpha = 1.8$ and 3.5 reflect, respectively, values encountered in the work on shear thinning fluids [13] and perturbed Newtonian fingering [11]. Furthermore, the saturation widths λ_m of fingers in those two instances are indicated (dot-dashed lines with symbols). We see that λ_m from our own experiments are in the same range as those from the previous studies, and that a parameter of $\alpha \approx 1.0$ would consistently explain our data as saturated fingers.

What determines λ_m in our case? It cannot be the tip radius of curvature approaching b, because the extent of every individual bubble is greater than that. In fact, the saturation mechanism is naturally explained by this very discreteness of the foam: As the crack outline is made up of individual bubbles with an average number of sides equal to five (by Euler's theorem), we can estimate a lower bound ρ_m for the radius of curvature by assuming that the three foremost nodes on the crack tip belong to two adjacent regular pentagonal bubbles; assuming these bubbles are of the same cross-sectional area as the initial hexagonal bubble (of side length 1) results in a pentagonal side-length of approximately 1.2289. The two edges on the crack outline will be separated by an angle of $4\pi/5$, from which simple geometry and parabola fitting through the leading three points then gives $\rho_m \approx 1.80$. In this discrete limit, we estimate the corresponding minimal crack width (14) as $\lambda_m \approx 0.394$ for $W = 22/b$, shown as the black dashed line on Fig. 7(b) and also illustrated in Fig. 8(c,d) below.

There remains an interesting difference between two groups of our data: the more regular and slightly thinner finger shapes for $\overline{\Delta P_d} \lesssim 0.26$, whose curvature and width are very close to these predicted minimum values, and the somewhat more irregular cracks for $\overline{\Delta P_d} \gtrsim 0.26$, which are slightly wider and whose

morphology fluctuates more during the propagation (compare the strong variation of $\rho(t)$ in Fig. 3(c) for $\overline{\Delta P_d} = 0.30$ with the regular behavior in Fig. 6(b) for $\overline{\Delta P_d} = 0.25$). This transition in behaviour around $\overline{\Delta P_d} \sim 0.26$ may be understood from the dynamics of the T1 processes that make up the crack propagation: After a T1 event, the newly generated edge has to lengthen to approximately average length L before the bubble arrangement can be called regular again. If this time to complete the T1 event is longer than the interval to the beginning of the following T1 transition, the individual events will influence each other and give rise to both stronger statistical fluctuations and to a less regular finger shape. In this regime, PBN positions and HPB orientations are no longer the result of merely quasistatic surface tension forces, but are co-determined by viscous forces, whose retarding influence on the motion is maximal for HPBs orientated perpendicular to the direction of motion. The net effect, thus, is that HPBs at the tip become oriented more perpendicularly to the motion, and therefore form a flatter crack tip. This qualitatively explains the increased ρ values and accompanying increased finger widths through (14) in this regime of larger $\overline{\Delta P_d}$.

5 Conclusions

We have shown that discrete network simulations of foam bubbles in a rectangular Hele-Shaw cell, invaded by air under an imposed pressure, give rise to crack structures very similar in morphology to that of viscous fingers. In further analogy to the viscous fingering case, the observed cracks appear to be of saturated width at large enough capillary number (where the crack width no longer follows the universal law (10)) in a regime known as anomalous fingering. Anomalous fingering occurs because of perturbations of the symmetry of the Saffman-Taylor fingering solution, and was also shown to occur in shear-thinning fluids.

As the morphology of the fingers in our network simulations (i.e., the width λ and tip curvature $1/\rho$) remains approximately constant over a considerable range of crack speeds, it is natural to assume that our simulations have reached the saturation regime of propagation. Interpreting the layer of bubbles between the plates of the Hele-Shaw cell as an effective medium, we find that this interpretation is indeed compatible with previous results on anomalous fingering. It is, in fact, expected that fingering in foams would be anomalous: First, in foams, there is an obvious mechanism breaking symmetry at the tip of the crack (or finger). The discreteness of individual bubbles will always lead to fluctuations in shape and curvature that do not allow for an ST selection of width (cf. Fig. 4 for the dynamically changing shape of the tip). Note that the presence of a bubble in front of the finger tip will induce the breaking of the shape symmetry in Newtonian fluids [32] – in a foam, there is always a bubble in front of the crack tip! Secondly, foams are non-Newtonian fluids with shear-thinning rheology, and the translation of our foam parameters into effective continuum parameters puts these systems in a regime in which anomalous fingering (with saturated width) has indeed been observed. That saturation is observed at a tip curvature of around $\bar{\rho} \approx 2$ is also understandable from the discrete bubble structure of the finger tip outline. A sharper tip cannot be realized in the network model, and thus this limit is analogous to the anomalous-fingering width limit in Newtonian fluids, where the limit is set by the two-dimensional continuum model breaking down [11]. The observed transition from completely regular, stable finger shapes at lower driving pressure to somewhat wider, more strongly fluctuating shapes at higher driving pressure can also be rationalized from the inherent time scales of the dynamics of discrete T1 processes. It should be noted that a slight increase in finger width with crack speed beyond saturation was also observed in the non-Newtonian fingering studies of [13] – it is possible that this effect can be similarly understood from inherent time scales of the non-Newtonian media.

It is encouraging that our network model, which was not developed with a continuum limit in mind, yields these results analogous to fingering experiments in fluids – it appears to confirm that effective rheology is the main determinant of this instability behavior, and that it can be realized with discrete entities. It also shows that the breakdown of the continuum description can be understood as a failure of

describing the interface by a smooth, two-dimensional geometry. Future simulations with a wider channel (thus enabling a larger ratio of tip ratio of curvature and bubble size) should explore this analogy further, and investigate whether there are further differences in the shape of the interface away from the tip, where yield-stress behavior should become important.

In a more general sense, our simulations explore the boundary between the failure of a solid (fracture) and the interfacial instability of a liquid (fingering). We find that the morphology and dynamics of the crack tip in a foam system can be, to a large extent, described by the formalisms developed by fluid dynamics, but with the network modeling elaborated here it is always possible to explore effects of elasticity, as well as possible effects of the microstructure of the bubbles. As many, if not most, of materials in applications are viscoelastic (this includes media in advanced oil recovery and hydraulic fracture applications [36]), studies such as the present one can give both fundamental and practical insight into the shape and dynamics of an interface between two media.

A Irregular crack morphology for larger driving pressures

Figure 8 explores the difference between the more regular finger shapes for $\overline{\Delta P_d} \lesssim 0.26$ and the more irregular cracks for $\overline{\Delta P_d} \gtrsim 0.26$. In particular, we examine the influence of the choice of spatial interval over which we average the width and radius of tip curvature. In Fig. 8(a) we plot the position of the crack tip as a function of time for four driving pressures ($\overline{\Delta P}_d = 0.2, 0.25, 0.3, 0.35$), highlighting three possible intervals for computing the steady crack speed ($30 \leq y_f \leq 55$, $35 \leq y_f \leq 60$, $40 \leq y_f \leq 65$). In Fig. 8(b) the mean normalised radius of curvature is plotted against the mean crack width for these three intervals. The trend is as in figure 7(b); for $\overline{\Delta P_d} \lesssim 0.26$ (filled shapes) the computed points cluster together very close to the analytical prediction (14). For $\overline{\Delta P_d} \gtrsim 0.26$ (open shapes) the data are again more scattered around the prediction (14), but in different patterns for each interval. We can therefore conclude that on average the crack shape resembles the anomalous finger shape, but there are deviations because the shape has not yet fully settled and due to the unsteady character of the measures of morphology.

We further examine the crack morphology for these four driving pressures, plotting the temporal change in the predicted crack width (Fig. 8c) and the crack tip radius of curvature (Fig. 8d). For $\overline{\Delta P_d} = 0.2$, $\overline{\Delta P_d} = 0.25$ and $\overline{\Delta P_d} = 0.35$ the crack width decreases fairly smoothly after the initial transient (Fig. 8c); for long times the mean crack width saturates close to the discrete limit λ_m identified above. The corresponding radius of curvature of the crack tip also decreases towards the discrete limit ρ_m (Fig. 8d), although we observe a brief increase in radius of curvature for $\overline{\Delta P_d} = 0.2$ at $t \approx 290$, similar to the sharp increase discussed in Fig. 4, which we attribute to the sensitivity in estimating the radius due to the discreteness of the crack outline. In Figs. 8(c,d) the region of each curve highlighted with symbols illustrates the interval used to compute the mean for $30 \leq y_f \leq 55$: for $\overline{\Delta P_d} = 0.2$ and $\overline{\Delta P_d} = 0.25$ the predictions in this interval are approaching the saturated limit, while the intervals for $\overline{\Delta P_d} = 0.3$ and $\overline{\Delta P_d} = 0.35$ are picking up effects from the initial transient. In particular, for $\overline{\Delta P_d} = 0.35$ saturation to the discrete limit occurs beyond $y_f = 55$, i.e. the time interval where the crack can be regarded as propagating steadily (compare Fig. 8a), so the result for the mean crack width must be interpreted with caution. For $\overline{\Delta P_d} = 0.3$ the crack width appears to be saturating to a much larger value than the others, while the radius of curvature eventually approaches the discrete limit (Fig. 8d). In this case the influence of the initial transient is much longer, with a narrower crack forming towards the tip for long times (see Fig. 3c). If we estimate the crack width using the area and length of a smaller portion of the crack the mean width is reduced and is more consistent with the other driving pressures, coming closer to the discrete limit.

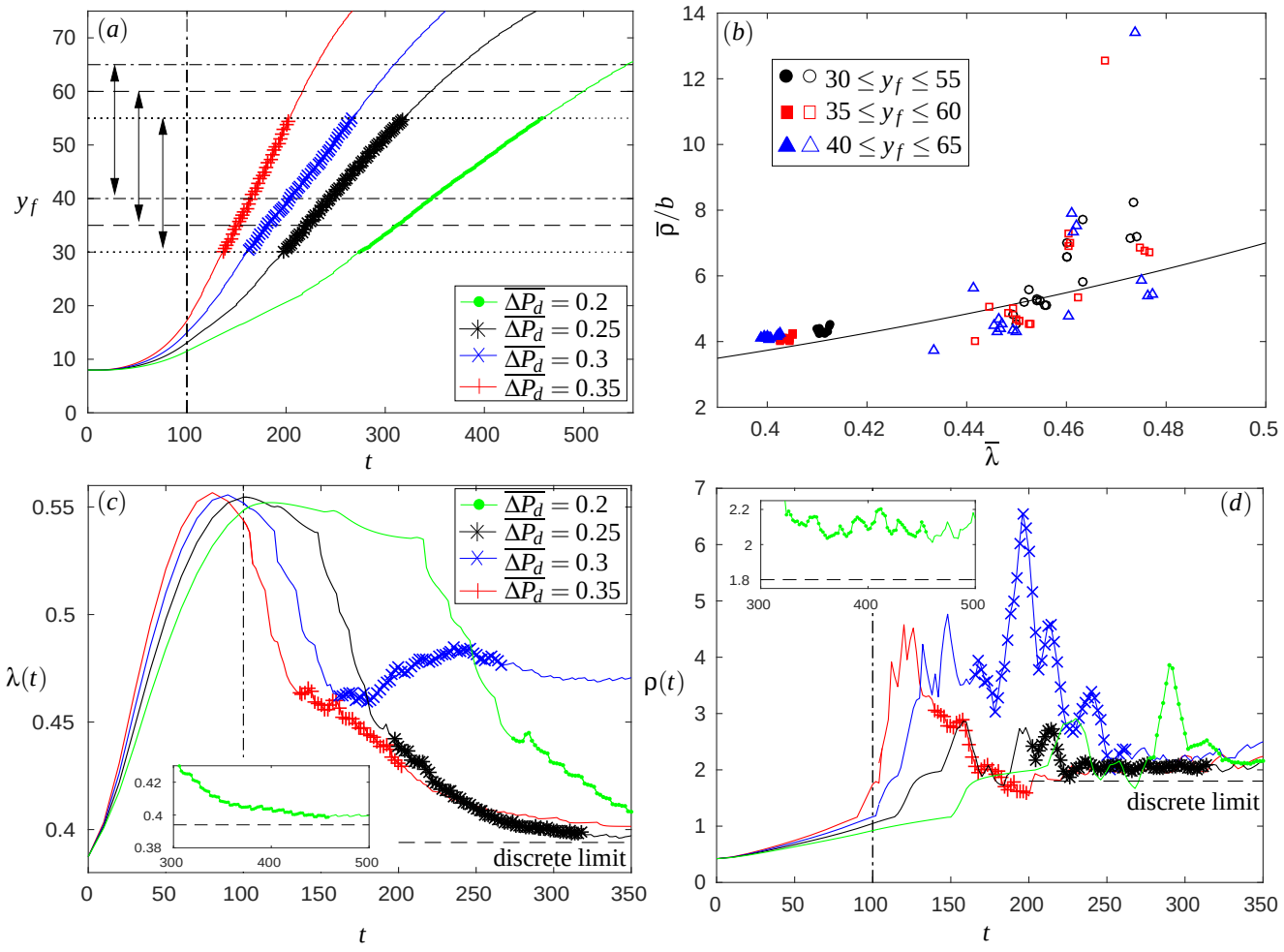

Figure 8: Comparison of foam fingering for a range of driving pressures: (a) temporal evolution of the position of the crack tip for $\overline{\Delta P_d} = 0.2$ (green, $\bullet$), $\overline{\Delta P_d} = 0.25$ (black, $*$), $\overline{\Delta P_d} = 0.3$ (blue, $\times$) and $\overline{\Delta P_d} = 0.35$ (red, $+$), showing the three possible spatial intervals; (b) the computed mean normalised crack tip radius of curvature plotted against the mean relative crack width for three spatial intervals, $30 \le y_f \le 55$ (filled and open black circles), $30 \le y_f \le 55$ (filled and open red squares), $30 \le y_f \le 55$ (filled and open blue triangles circles), where in each case filled symbols are for $\overline{\Delta P_d} \le 0.26$ and open symbols are for $\overline{\Delta P_d} > 0.26$; (c) temporal evolution of the mean crack width for the four driving pressures considered in (a) with the same colour scheme; (d) temporal evolution of the mean crack tip radius of curvature for the four driving pressures considered in (a) with the same colour scheme. The region highlighted by symbols in (a), (c) and (d) illustrates the region where the crack tip is in the interval $30 \le y_f \le 55$. The dashed lines in (c), (d) represent the discrete limit values λ_m and ρ_m, respectively. The insets in (c), (d) illustrate the long-time behaviour for $\overline{\Delta P_d} = 0.20$.

References

[1] L. Bragg and J. F. Nye. A dynamical model of a crystal structure. *Proc. Roy. Soc. A*, 190(1023):474–481, 1947.

[2] A. Gouldstone, K. J Van Vliet, and S. Suresh. Nanoindentation: Simulation of defect nucleation in a crystal. *Nature*, 411(656), 2001.

[3] K.J. Van Vliet, J. Li, T. Zhu, S. Yip, and S. Suresh. Quantifying the early stages of plasticity through nanoscale experiments and simulations. *Phys. Rev. B*, 67:104105, 2003.

[4] R. Farajzadeh, A. Andrianov, R. Krastev, G.J. Hirasaki, and W.R. Rossen. Foam–oil interaction in porous media: Implications for foam assisted enhanced oil recovery. *Adv. Coll. Interf. Sci.*, 183:1–13, 2012.

[5] J. Banhart. Manufacture, characterisation and application of cellular metals and metal foams. *Prog. Mater. Sci.*, 46(6):559–632, 2001.

[6] S. Farrokhpay. The significance of froth stability in mineral flotation: A review. *Adv. Colloid Interf. Sci.*, 166(1):1–7, 2011.

[7] S. Arif, J.C. Tsai, and S. Hilgenfeldt. Speed of crack propagation in dry aqueous foam. *Eur. Phys. Lett.*, 92(3):38001, 2010.

[8] S. Arif, J. C. Tsai, and S. Hilgenfeldt. Spontaneous brittle-to-ductile transition in aqueous foam. *J. Rheol.*, 56:485, 2012.

[9] S. Hilgenfeldt, S. Arif, and J.C. Tsai. Foam: a multiphase system with many facets. *Phil. Trans. Royal Soc. A*, 366:2145–2159, 2008.

[10] P.G. Saffman and G.I. Taylor. The penetration of a fluid into a porous medium or Hele-Shaw cell containing a more viscous liquid. 245(1242):312–329, 1958.

[11] M. Rabaud, Y. Couder, and N. Gerard. Dynamics and stability of anomalous Saffman–Taylor fingers. *Phys. Rev. A*, 37(3):935, 1988.

[12] M.B. Poiré, E.C. Ben Amar. Finger behavior of a shear thinning fluid in a hele-shaw cell. *Phys. Rev. Lett.*, 81(10):2048, 1998.

[13] A. Lindner, D. Bonn, E.C. Poiré, M. Ben Amar, and J. Meunier. Viscous fingering in non-newtonian fluids. *J. Fluid Mech.*, 469:237–256, 2002.

[14] I. Cantat and R. Delannay. Dynamical transition induced by large bubbles in two-dimensional foam flows. *Phys. Rev. E*, 67(3):031501, 2003.

[15] I. Cantat and R. Delannay. Dissipative flows of 2d foams. *Eur. Phys. J. E*, 18(1):55–67, 2005.

[16] S.S. Park and D.J. Durian. Viscous and elastic fingering instabilities in foam. *Phys. Rev. Lett.*, 72(21):3347, 1994.

[17] I. Ben Salem, I. Cantat, and B. Dollet. Response of a two-dimensional liquid foam to air injection: swelling rate, fingering and fracture. *J. Fluid Mech.*, 714:258–282, 2013.

[18] A. Lindner, P. Coussot, and D. Bonn. Viscous fingering in a yield stress fluid. *Phys. Rev. Lett.*, 85(2):314, 2000.

[19] P.S. Stewart, S.H. Davis, and S. Hilgenfeldt. Microstructural effects in aqueous foam fracture. *J. Fluid Mech.*, 785:425–461, 2015.

[20] P.S. Stewart and S.H. Davis. Dynamics and stability of metallic foams: network modelling. *J. Rheol.*, 56:543, 2012.

[21] P.S. Stewart and S.H. Davis. Self-similar coalescence of clean foams. *J. Fluid Mech.*, 722:645–664, 2013.

[22] P.S. Stewart, S.H. Davis, and S. Hilgenfeldt. Viscous Raleigh–Taylor instability in aqueous foams. *Coll. Surf. A*, 436:898–905, 2013.

[23] I. Cantat. Liquid meniscus friction on a wet plate: Bubbles, lamellae, and foams. *Phys. Fluids*, 25(3):031303, 2013.

[24] F.P. Bretherton. The motion of long bubbles in tubes. *J. Fluid Mech.*, 10:166–188, 1961.

[25] D.L. Weaire and S. Hutzler. *The Physics of Foams*. Oxford University Press, 2001.

[26] S. F. Edwards and D. V. Grinev. Statistical mechanics of stress transmission in disordered granular arrays. *Phys. Rev. Lett.*, 82(26):5397, 1999.

[27] L.B. Freund. *Dynamic fracture mechanics*. Cambridge university press, 1998.

[28] P. Tabeling, G. Zocchi, and A. Libchaber. An experimental study of the Saffman-Taylor instability. *J. Fluid Mech.*, 177:67–82, 1987.

[29] Y. Couder. On the analogy of anomalous viscous fingers with crystalline dendrites. In *Propagation in Systems Far from Equilibrium*, pages 63–77. Springer, 1988.

[30] J.W. McLean and P.G. Saffman. The effect of surface tension on the shape of fingers in a Hele–Shaw cell. *J. Fluid Mech.*, 102:455–469, 1981.

[31] G. Zocchi, B. E. Shaw, A. Libchaber, and L. P. Kadanoff. Finger narrowing under local perturbations in the Saffman-Taylor problem. *Phys. Rev. A*, 36(4):1894, 1987.

[32] Y. Couder, N. Gerard, and M. Rabaud. Narrow fingers in the Saffman–Taylor instability. *Phys. Rev. A*, 34(6):5175, 1986.

[33] S. Cohen-Addad, R. Höhler, and O. Pitois. Flow in foams and flowing foams. *Ann. Rev. Fluid Mech.*, 45(1):241, 2013.

[34] N.D. Denkov, V. Subramanian, D. Gurovich, and A. Lips. Wall slip and viscous dissipation in sheared foams: Effect of surface mobility. *Coll. Surf. A*, 263(1):129–145, 2005.

[35] A.M. Kraynik and M.G. Hansen. Foam and emulsion rheology: A quasistatic model for large deformations of spatially-periodic cells. *J. Rheol.*, 30(3):409–439, 1986.

[36] R. Barati and J.-T. Liang. A review of fracturing fluid systems used for hydraulic fracturing of oil and gas wells. *J. Appl. Polymer Sci.*, 131(16), 2014.